

Resonant modes in metal/insulator/metal metamaterials: An analytical study on near-field couplingsShaojie Ma,¹ Shiyi Xiao,¹ and Lei Zhou^{1,2,*}¹*State Key Laboratory of Surface Physics, Key Laboratory of Micro and Nano Photonic Structures (Ministry of Education) and Physics Department, Fudan University, Shanghai 200433, China*²*Collaborative Innovation Center of Advanced Microstructures, Fudan University, Shanghai 200433, China*
(Received 8 September 2015; revised manuscript received 24 December 2015; published 13 January 2016)

Metamaterials (MTMs) in a metal/insulator/metal (MIM) configuration have drawn much attention recently, but the resonances in such systems are still not fully understood. Here, we employ a rigorous mode expansion method to analytically study the resonance properties of a model MIM MTM where the top metallic layer consists of an array of metallic stripes. Our analyses, supported by full-wave simulations and microwave experiments, provide a unified platform to understand the resonances in such systems, in which two previously established models are found valid only at certain extreme conditions. In particular, the resonance in such a system undergoes a transition from a vertical Fabry-Pérot type to a transverse type as the spacer thickness shrinks, and the resonance frequency saturates at a particular value in the thin-spacer limit. Finally, we derive a set of analytical formulas to describe how the essential properties (i.e., resonance frequency and quality factor) of the resonance depend on the structural details of the system and verify these analytical relationships by full-wave simulations in MIM systems with complex microstructures.

DOI: [10.1103/PhysRevB.93.045305](https://doi.org/10.1103/PhysRevB.93.045305)**I. INTRODUCTION**

Metamaterials (MTMs), artificial composites consisting of subwavelength microstructures with tailored electromagnetic (EM) responses, exhibit strong abilities to manipulate EM waves, leading to novel physical effects such as negative refraction [1,2], super/hyper imaging [3,4], polarization control [5–7], perfect absorption [8–10], and more recently the anomalous EM wave refraction/reflection [11–13] and other related effects [14–16]. One important achievement in MTM research is the artificial optical magnetism, realized by carefully designed resonant microstructures [17–19]. In addition to split ring resonators [1,11,17] discovered previously, such magnetic MTM structures also include a category of systems in a metal/insulator/metal (MIM) configuration, which typically combine two identical electric resonators [18] or one electric resonator with a metallic sheet [5–10,12–16,19].

In addition to using such MIM structures in photonic applications ranging from reflectance control [8–10] to wavefront control [5–7,11–16], people also developed several theories to understand the nature of the resonances in these systems [19–22]. Previously, a commonly accepted physical picture was that the electric currents (induced by external EM fields) flow in opposite directions on two metallic layers due to the near-field coupling (NFC) between two layers, so that the whole system behaves as a magnetic medium characterized by an effective permeability μ [19,20]. However, as the spacer thickness becomes large, a different picture was established in Ref. [21], where the author treated two metallic layers as metasurfaces with certain transmission/reflection characteristics and then used a multiple-scattering technique to study the transmission/reflection properties of the whole system. In such an interference model, the “magnetic” resonance does not necessarily exist in the system, and all physical effects can be alternatively understood based on Fabry-Pérot (FP) interferences among multiply scattered waves [21]. Obviously,

the key difference between these two theories is whether or not the NFC between two metallic layers plays an important role in determining the resonances generated in such systems, or equivalently speaking, whether the two metallic layers can be treated *independently* or they have to be studied as a whole. It is clear that these two pictures work separately for MIM systems with different spacers [5–21], and a transition between these two types of resonance was also noted as the spacer thickness increases [22]. However, so far a *unified* framework that can work for *arbitrary* spacer thicknesses and can describe how the resonance evolves as the spacer thickness changes is still lacking and is highly desired.

In this paper, we address these issues by analytically studying a model MIM with a simple geometry, which contains a periodic array of metallic stripes coupled with a metallic sheet through a dielectric spacer [see Fig. 1(a)]. Analytical solutions on such a simple structure can shed light on the underlying physics in more general situations. To achieve this end, we first employ a rigorous mode-expansion-method (MEM) to study the scattering properties of such a model and validate the MEM by full-wave simulations and microwave experiments (Sec. II). We next derive from the rigorous MEM two sets of analytical formulas to describe the most essential properties of the resonance, including the resonance frequency and its associated quality (Q) factor, under the thin-spacer and thick-spacer limits, respectively (Sec. III). These formulas can validate two previously established models under certain conditions and reveal the important role of the NFC in determining the resonance characteristics as the spacer thickness is smaller than a critical value. In particular, we show that the NFC can drive the resonance to transit from a vertical FP-like to a transverse type as the spacer thickness decreases. We next employ our analytical formulas to discuss high-order resonances in MIM systems with even thicker spacers and show that interesting phenomena can emerge due to interplays between different mechanisms (Sec. IV). Section V is devoted to extending these analytical formulas to general simulations with complex microstructures. Finally, we conclude our paper in Sec. VI.

*phzhou@fudan.edu.cn

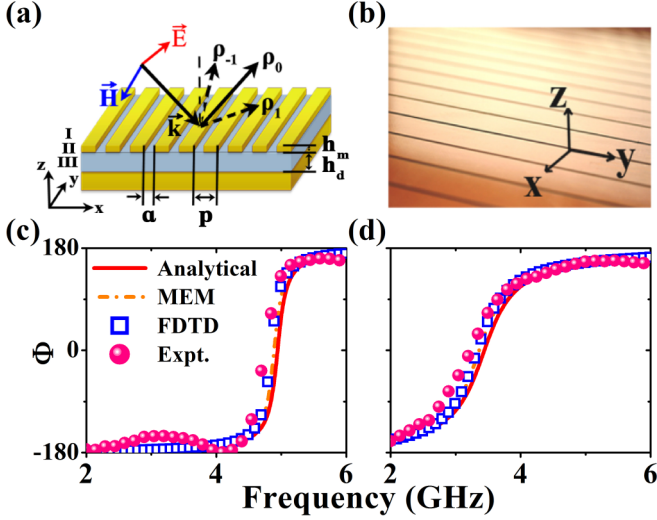


FIG. 1. (a) Schematics of the MIM MTM under study, which contains a periodic array of metallic stripes and a continuous metal sheet separated by a dielectric spacer. (b) Picture of a fabricated microwave sample. Reflection-phase (Φ) spectra obtained by microwave experiments (solid circles), FDTD simulations (open squares), MEM (dashed lines), and simplified analytical model (solid lines) for two systems with the lateral geometry fixed as $a = 1$ mm, $p = 15$ mm, $h_m = 0.035$ mm and different spacer thickness (c) $h_d = 0.5$ mm, (d) $h_d = 3$ mm. The permittivity of the spacer is $\epsilon_d = 4.3$.

II. DEVELOPMENT OF THE RIGOROUS MEM

The geometry of our model is schematically shown in Fig. 1(a). The thicknesses of the metallic stripes and the dielectric spacer are h_m and h_d , respectively. The periodicity of the stripe array is p , while the gap between two adjacent stripes is a . The structure is invariant along the y direction. In this paper, we are primarily interested in the low-frequency domain where metals can be treated as perfect electric conductors (PEC). With a continuous metal sheet on the back, the MIM structure does not allow EM wave transmission. Therefore, we only study the reflection properties of the system under illuminations by a transverse-magnetic (TM) polarized plane wave with $\vec{H} \parallel \hat{y}$. Here, the $z = 0$ plane is defined at the top surface of the spacer layer.

We follow the standard MEM [23–25] to expand EM waves in different regions to linear combinations of eigenmodes in those regions. In region I occupied by air above the system, we can expand the \mathbf{E} field as

$$\vec{E}^I = \vec{E}_0^{\text{PW},-} + \sum_n \rho_n \vec{E}_n^{\text{PW},+}, \quad (1)$$

where $\vec{E}_0^{\text{PW},-}$ represents the TM-polarized incident plane wave (PW) with parallel wave vector $k_{0,x}$, and $\vec{E}_n^{\text{PW},+}$ denotes the reflected PW propagating along the n th diffraction channel (with $k_{n,x}^I = k_{0,x} + nG$ where $G = 2\pi/p$ and $n = 0, \pm 1, \dots$) with ρ_n being the corresponding reflection coefficient. Here, \pm denotes the sign in front of k_z , and the parallel \mathbf{E} component in the n th eigenmode is $\vec{E}_{n,\parallel}^{\text{PW},\pm} = 1/\sqrt{p} \cdot \exp(ik_{n,x}^I x) \cdot \exp[\pm ik_{n,z}^I (z - h_m)] \hat{x}$. Meanwhile, in region II where the metallic stripes are located, \mathbf{E} field can only exist inside those air slits and can be expanded as linear combinations of a series

of waveguide modes inside the slits. Specifically, inside the slit centered at x_j , we can write the \mathbf{E} field as

$$\begin{aligned} \vec{E}^{\text{II}} = & \sum_q (a_q^+ \vec{E}_q^{\text{WG},+} + a_q^- \vec{E}_q^{\text{WG},-}) \\ & \cdot e^{ik_{0,x} x_j}, \quad |x - x_j| < a/2, \end{aligned} \quad (2)$$

where $\vec{E}_q^{\text{WG},\pm}$ denotes the q th waveguide mode travelling along $\pm z$ directions with a_q^\pm being the corresponding expansion coefficients. The parallel \mathbf{E} component in the q th waveguide mode is $\vec{E}_{q,\parallel}^{\text{WG},\pm} = 1/2\sqrt{a} \cdot [\exp(ik_{q,x}^{\text{II}} x) + (-1)^q \exp(-ik_{q,x}^{\text{II}} x)] \cdot \exp(\pm ik_{q,z}^{\text{II}} z) \hat{x}$ (with $k_{q,x}^{\text{II}} = q \cdot \pi/a$). A phase factor $e^{ik_{0,x} x_j}$ is purposely added to the expression in accordance with the Bloch condition. We now consider region III which is the dielectric spacer sandwiched by two metallic layers. Electromagnetic eigenmodes in this region are similar to those in region I except that, here, the space is occupied by a dielectric medium with permittivity ϵ_d . Specifically, we can write the \mathbf{E} field as

$$\vec{E}^{\text{III}} = \sum_m (c_m^+ \vec{E}_m^{\text{SC},+} + c_m^- \vec{E}_m^{\text{SC},-}), \quad (3)$$

where c_m^\pm are the expansion coefficients for the m th scattering mode with normalized wave functions $\vec{E}_{m,\parallel}^{\text{SC},\pm} = 1/\sqrt{p} \cdot \exp(ik_{m,x}^{\text{III}} x) \cdot \exp(\pm ik_{m,z}^{\text{III}} z) \hat{x}$. In all these regions, \mathbf{H} fields can be derived from the corresponding \mathbf{E} fields employing Maxwell's equations. In addition, the perpendicular wave vectors are determined by $(k_{n,x}^i)^2 + (k_{n,z}^i)^2 = \epsilon_i \cdot (\omega/c)^2$, where ω and c denote the frequency and speed of light, respectively, and ϵ_i is the relative permittivity in the i th region ($i = \text{I, II, III}$, and $\epsilon_1 = \epsilon_2 = 1$, $\epsilon_3 = \epsilon_d$). Matching the tangential components of \mathbf{E} and \mathbf{H} fields at three interfaces between adjacent regions and employing the orthonormal conditions of these eigenmodes, we get the following set of coupled linear equations (Appendix A):

$$\begin{aligned} \rho_n + \delta_{n,0} &= \sum_q S_{nq}^{(1,2)} [a_q^+ \exp(ik_{q,z}^{\text{II}} h_m) + a_q^- \exp(-ik_{q,z}^{\text{II}} h_m)] \\ &+ \sum_n S_{qn}^{(2,1)} Y_n^I [\rho_n - \delta_{n,0}] \\ &= Y_q^{\text{II}} [a_q^+ \exp(ik_{q,z}^{\text{II}} h_m) - a_q^- \exp(-ik_{q,z}^{\text{II}} h_m)] \\ c_m^+ + c_m^- &= \sum_q S_{mq}^{(3,2)} [a_q^+ + a_q^-] \\ &+ \sum_m S_{qm}^{(2,3)} Y_m^{\text{III}} [c_m^+ - c_m^-] = Y_q^{\text{II}} [a_q^+ - a_q^-] \\ c_m^+ \exp(-ik_{m,z}^{\text{III}} h_d) + c_m^- \exp(ik_{m,z}^{\text{III}} h_d) &= 0, \end{aligned} \quad (4)$$

to determine those expansion coefficients (i.e., ρ_n, a_q^\pm, c_m^\pm). Here, $Y_n^i = \omega \epsilon_i / k_{n,z}^i$ denotes the admittance for the n th mode in the i th region, $S_{nq}^{(1,2)} = \int_{-a/2}^{a/2} (\vec{E}_n^{\text{PW}})^* \cdot \vec{E}_q^{\text{WG}} dx = (S_{qn}^{(2,1)})^*$ denotes the overlapping integral between the n th diffracting PW in region I and the q th waveguide mode inside the air slit, and $S_{mq}^{(3,2)} = \int_{-a/2}^{a/2} (\vec{E}_m^{\text{SC}})^* \cdot \vec{E}_q^{\text{WG}} dx = (S_{qm}^{(2,3)})^*$ has a similar definition.

We can solve Eq. (4) to get all expansion coefficients $\{\rho_n, a_q^\pm, c_m^\pm\}$. Among these parameters, the specular reflection coefficient ρ_0 is the most important one since all higher order diffraction modes (in region I) are evanescent waves. Although in principle infinite number of modes should be taken into account in solving Eq. (4), practically about 5 to 10 modes in each region are enough to ensure the computational convergence. Since we neglect losses, our system is always totally reflective, and thus $|\rho_0| = 1$. However, the phase Φ of ρ_0 can exhibit nontrivial dependence on frequency $f = \omega/2\pi$, which is the key property that we are interested in.

Dashed lines in Figs. 1(c) and 1(d) are the MEM-calculated reflection-phase spectra (i.e., $\Phi(f)$), for two model systems with the same lateral geometry but with different spacer thicknesses. For both systems, the reflection phase changes continuously from -180° to 180° as frequency increases and becomes exactly zero at a particular frequency (i.e., the resonance frequency). The in-phase reflection was one of the key properties of such systems [19]. However, we note that the resonance properties of two systems are quite different, even though these two systems share the same lateral geometry. Obviously, the resonance appears at a higher frequency in the thinner system [Fig. 1(c)]. What is more, the resonance bandwidth is also significantly narrowed when the spacer is thinner, implying the higher Q factor of the resonance.

We performed finite-difference-time-domain (FDTD) simulations and microwave experiments to justify the developed MEM. We fabricated two realistic samples based on the geometrical parameters adopted in the MEM [see Fig. 1(b) for the picture of a fabricated sample]. In our experiments, we illuminated these systems by TM-polarized microwaves (with $\vec{H} \parallel \hat{y}$) using a horn antenna and then measured the reflected signals through another identical horn antenna. Both horn antennas were connected to a vector-field analyzer (Agilent E8362C). Since we cannot measure the normal-incidence spectrum where two antennas will touch each other, we set the incident angle at 10° , but all FDTD simulations were performed under normal-incidence condition [26]. The measured signals were normalized against a reference signal, obtained through replacing the sample by a metal plate with the same size. The measured reflection-phase spectra are shown as solid circles in Figs. 1(c) and 1(d), together with the corresponding FDTD simulation results (open squares). Excellent agreements among MEM, FDTD, and experimental results validated the developed MEM.

III. ANALYTICAL FORMULAS FOR THE RESONANCE BEHAVIORS

Although the MEM established in the last section is rigorous, it involves too complicated mathematics which obscured the underlying physics. In this section, we simplify the complicated formalism under certain approximations to derive a set of closed-form analytical formulas, which can well describe the most essential properties (the resonance frequency and Q factors) of the resonances in such structures. These analytical formulas not only clearly illustrate the physical origins of the resonances in different regimes, but also reveal

when and why previous theories are valid for such MIM structures.

A. General formulas

We consider the situation with $a/p \ll 1$ (thin slit), $p/\lambda \ll 1$ (subwavelength microstructure), and $h_m/\lambda \ll 1$ (thin metal film). Under the first two conditions, we can simplify Eq. (4) by retaining only the fundamental modes in regions I and II, which are the specular-reflection mode in air and the transverse EM (TEM) mode inside the slit. Such a single-mode approximation is justified by the following two facts: (1) the higher order diffraction modes in air region are all evanescent waves since $p/\lambda \ll 1$, and (2) the couplings involving higher order modes inside the slit (i.e., $S_{nq}^{(1,2)}$ and $S_{mq}^{(3,2)}$ with $q \neq 0$) are much smaller than those involving only the fundamental one (i.e., $S_{n0}^{(1,2)}$ and $S_{m0}^{(3,2)}$) in the limit of $a/p \rightarrow 0$. However, all higher order modes in the spacer (region III) must be retained, even though they are all evanescent waves, and we will show that these modes play very important roles here. The third condition $h_m/\lambda \rightarrow 0$ is generally satisfied in practically fabricated systems working in low frequency domains (e.g., gigahertz and terahertz domains), where the metal's skin depth is very small, and thus a metal film does not need to be very thick. Under this condition, we can neglect the propagation phase of the TEM waveguide mode by assuming $h_m = 0$.

Under these approximations, we get a rigorous solution for Eq. (4) (see Appendix A for derivations), in which the specular reflection coefficient ρ_0 is

$$\rho_0 = \frac{1 - Y_{\text{eff}}}{1 + Y_{\text{eff}}}, \quad (5)$$

where

$$Y_{\text{eff}} = i \cdot \sum_m \frac{Y_m^{\text{III}}}{Y_0^{\text{I}}} \cdot \frac{|S_{m0}^{(3,2)}|^2}{|S_{00}^{(1,2)}|^2} \cdot \cot(k_{m,z}^{\text{III}} h_d), \quad (6)$$

can be viewed as the effective admittance of the system. Equations (5) and (6) reveal that all diffraction channels in region III can contribute to the response of the whole system, and $\cot(k_{m,z}^{\text{III}} h_d)$ describes the multiple scatterings between two metallic layers, while $\frac{Y_m^{\text{III}}}{Y_0^{\text{I}}} \cdot \frac{|S_{m0}^{(3,2)}|^2}{|S_{00}^{(1,2)}|^2}$ describes the *effective* impedance contrast between the m th mode inside the cavity and the 0th external mode in air. To justify Eq. (5), we employ it to calculate the responses of two model systems studied in last section. Solid lines in Figs. 1(c) and 1(d) reveal that our analytical formula can well reproduce the full-wave simulations and the rigorous MEM results.

We now derive an analytical formula for the resonance frequency of such system. Obviously, the system is resonant at frequencies where in-phase reflections occur, which correspond to the condition $Y_{\text{eff}} = 0$ [see Eq. (5)], that is

$$\sum_m Y_m^{\text{III}} |S_{m0}^{(3,2)}|^2 \cot(k_{m,z}^{\text{III}} h_d) = 0. \quad (7)$$

In general, Eq. (7) is a transcendental equation that has to be solved numerically. Solid line in Fig. 2(a) depicts how the wavelength λ_0 of the fundamental resonance varies as

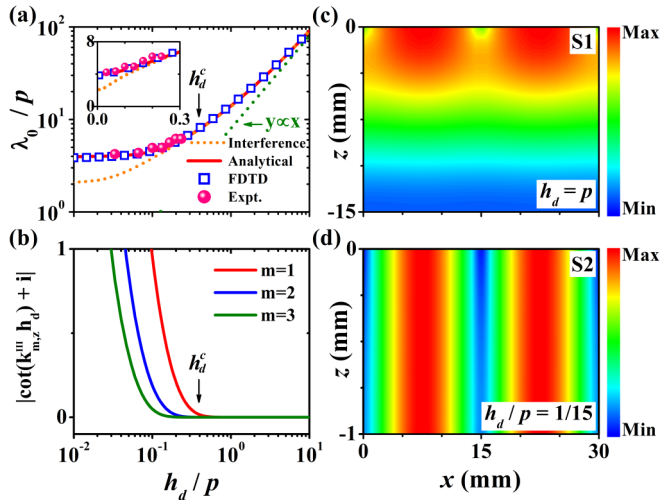


FIG. 2. (a) Fundamental resonance wavelength λ_0 of MIM systems as functions of the spacer thickness h_d , obtained by microwave experiments (solid circles), FDTD simulations (open squares), our analytical formula (solid line), and interference model (dotted line). Inset shows a zoomed view of the region $h_d/p \in [0, 0.3]$. (b) Values of $|\cot(k_{m,z}^{III} h_d) + i|$ for the first three evanescent modes as functions of h_d . FDTD-calculated $\text{Re}(H_y)$ field distributions on an arbitrary x - z plane in MIM systems with (c) $h_d = 15$ mm, $f_0 = 5.27$ GHz and (d) $h_d = 1$ mm, $f_0 = 4.54$ GHz, corresponding to resonances labeled by S1 and S2 specified in Fig. 5(b). Other parameters of the MIM systems are fixed as $a = 1$ mm, $p = 15$ mm, $h_m = 0.035$ mm, and $\varepsilon_d = 4.3$.

a function of h_d , obtained by numerically solving Eq. (7) for a series of systems with $h_m = 0.035$ mm, $a = 1$ mm, $p = 15$ mm fixed. These results are in excellent agreement with FDTD simulations (open squares) for all systems studied. Meanwhile, we also employ the interference model developed in Ref. [21] to study the same set of samples and depict the calculated results in the same figure as a dotted line. We find the interference model agrees well with the FDTD results only when h_d is thick enough. In particular, the fact that λ_0 depends almost linearly on h_d in the large- h_d region implies the FP nature of the resonance, in consistency with the interference model [21]. However, the discrepancy between two theories becomes significant when h_d is smaller than a critical thickness. In such a region, λ_0 obviously deviates from the linear h_d dependence but rather exhibits an intriguing saturation behavior in the limit of $h_d \rightarrow 0$. Finally, such resonance-saturation behavior has been verified by our microwave experiments, as shown by the solid circles in Fig. 2(a).

B. Analytical solutions for resonance frequency under two extreme conditions

To understand the inherent physics underlying the discrepancy in different spacer thickness regions, we analyzed Eq. (7) under two extreme conditions, i.e., $h_d/\lambda \gg 1$ and $h_d/\lambda \ll 1$.

Consider the limit $h_d/\lambda \gg 1$ first. Since all higher order diffraction modes are evanescent (i.e., $k_{m,z}^{III}$ are purely imaginary for $m \neq 0$), they all die off in the multiple scatterings, and therefore, we have $\cot(k_{m,z}^{III} h_d) \rightarrow -i$ for all the $m \neq 0$

terms. Meanwhile, only the fundamental mode (with a real $k_{0,z}^{III}$) survives in the multiple scatterings, and it is this h_d -dependent term $\cot(k_{0,z}^{III} h_d)$ that dominates the thickness dependence of λ_0 . Explicitly, put the limiting expressions $\cot(k_{m,z}^{III} h_d) = -i$ (for $m \neq 0$) into Eq. (7), we find that now λ_0 should be determined by

$$k_{0,z}^{III} h_d - \cot^{-1} \left(i \sum_{m \neq 0} Y_m^{III} |S_{m0}^{(3,2)}|^2 / Y_0^{III} |S_{00}^{(3,2)}|^2 \right) = l\pi, \quad l = 0, 1, 2, \dots \quad (8)$$

Equation (8) shows clearly that the resonance under the $h_d/\lambda \gg 1$ condition is a FP-like one, in consistency with the picture set up in Ref. [21]. Obviously, the term $\phi = k_{0,z}^{III} h_d$ in Eq. (8) must come from the propagation phase of the fundamental mode, while the second term is a surface-related term which can be interpreted as the reflection phase at the top metallic layer. Such a surface correction term is modified by the high-order evanescent modes generated at the surfaces, which in turn also slightly shift the resonance frequency. We note that multiple scatterings of high-order terms can also be incorporated following the method developed in Ref [27].

Figure 2(c) shows the field distribution of a typical resonance (with $l = 1$) obtained by solving Eq. (8). We find that high-order evanescent waves quickly die off as they leave the top metallic layer, and the field pattern exhibits a clear feature of vertical FP-like resonance. The high-order evanescent waves only modulate the near-field distributions at the top surface, which in turn modify the phase of the fundamental mode radiated from the surface.

We now consider another limit $h_d/\lambda \ll 1$. In this case, all modes do *not* die off. We expand the function $\cot(k_{m,z}^{III} h_d)$ to Laurent-Taylor series and retain only the leading contributions, i.e., $\cot(k_{m,z}^{III} h_d) \rightarrow (k_{m,z}^{III} h_d)^{-1}$. Put the above result into Eq. (7), we find the following equation

$$\sum_m (k_{m,z}^{III})^{-2} |S_{m0}^{(3,2)}|^2 = 0, \quad (9)$$

to determine the resonance frequency in the limit of $h_d \rightarrow 0$. Equation (9) is remarkable, since it reveals many new physics that were usually overlooked previously. First of all, we note Eq. (9) yields an h_d -independent resonance solution, which is in consistency with both FDTD and experimental results [see Fig. 2(a)]. Second, the physical origin of such a saturation behavior can be clearly understood from the derivation of Eq. (9). In the limit of $h_d \rightarrow 0$, all modes in Region III, no matter whether they are propagating or evanescent, exhibit the same $(h_d)^{-1}$ dependence in the multiple scattering processes. Therefore, the final resonance frequency does not exhibit any h_d dependence since the common h_d -dependent terms are factored out. Third, we note that high-order evanescent waves play a very important role to couple two metallic layers together in this limit, and it is no longer valid to implement the interference model which assumes that high-order evanescent waves only contribute a surface reflection-phase correction. In addition, since high-order evanescent waves (with nonzero parallel wave vectors) play crucial roles in establishing the resonant mode, we expect the field pattern to exhibit a lateral resonance feature rather than the vertical FP one.

The above physical understandings are fully supported by the FDTD simulated field distribution, depicted in Fig. 2(d) for a typical resonant mode in this region. The nearly z -invariant field evolution and the clear standing wave characteristics in the lateral direction are the direct proof of the “lateral resonance” in the limit of $h_d \rightarrow 0$. Such a picture is in the same spirit of a previous “magnetic resonance” argument [19], where the resonance is governed essentially by the lateral pattern rather than the spacer thickness.

Now that we have derived two analytical formulas [i.e., Eqs. (8) and (9)], valid respectively at two extreme conditions, we turn to check the intermediate regime to see how the resonance evolves from a FP one to a transverse one as h_d decreases. In deriving Eq. (8), we have assumed that only the fundamental mode in Region III is alive and all high-order modes die off in the multiple scattering processes. However, this assumption is only valid when the condition $h_d/\lambda \gg 1$ is strictly satisfied. As a quantitative estimation, we numerically solved Eq. (7), which is valid for arbitrary h_d , to get the values of $\cot(k_{m,z}^{\text{III}} h_d)$ for higher order modes. As shown in Fig. 2(b), while indeed we have $\cot(k_{m,z}^{\text{III}} h_d) \rightarrow -i$ in the limit of $h_d/\lambda \rightarrow \infty$, the deviations of $\cot(k_{m,z}^{\text{III}} h_d)$ from their limiting value $-i$ are significantly enhanced as h_d decreases. In particular, when h_d is smaller than a critical value $h_d^c = \text{Im}(k_{1,z}^{\text{III}})^{-1}$, which is identical to the decay length of the first evanescent mode, the first high-order mode can no longer be dropped [evidenced by the large deviation of $\cot(k_{1,z}^{\text{III}} h_d)$ from and $-i$, see Fig. 2(b)], which explains why the true h_d dependence of λ_0 starts to deviate significantly from the interference model [see Fig. 2(a)]. As h_d is further reduced, more and more high-order evanescent modes should be included in forming the resonance, making the final resonance wavelength deviating from the interference model more significantly. It is these high-order modes that gradually drive the resonance to transit from a FP one to a lateral one.

C. Analytical solutions for the Q factor under two extreme conditions

To fully understand the nature of a resonance, we need to also know the Q factor of the resonance in addition to the resonance frequency. The Q factor of a resonance is defined as the ratio between the total energy U stored inside the system and the energy P_r dissipated from the device during a time oscillation circle. Since we neglect material losses in this paper, we only need to consider the dissipation due to radiation. The time-averaged total energy $\langle U \rangle$ is obtained by summing up all EM energies (including both electric and magnetic parts) stored inside a unit-cell volume of the cavity, which is

$$\langle U \rangle = \frac{1}{4} \text{Re} \left[\int_{\text{u.c.}} d\tau (\varepsilon_d \varepsilon_0 E_x^* \cdot E_x + \mu_0 H_y^* \cdot H_y + \mu_0 H_z^* \cdot H_z) \right]. \quad (10)$$

Here, we have neglected the energy stored inside the air slits thanks to the thin film approximation. Now that the scattering problem of our system has been rigorously solved in Sec. II, Eq. (10) can be analytically worked out (see Appendix B). Meanwhile, P_r has to be treated with care. A naïve expectation

is that P_r should be proportional to the reflectance $|\rho_0|^2$. However, a careful analysis indicates that this is not correct, since the reflected wave actually contains two parts, one corresponding to the wave radiated from the excited resonance at a rate ρ_r , and another corresponding to the wave that is directly reflected back by the nonresonant background (PEC in our case) at a rate ρ_d . Therefore, the dissipation power P_r truly owing to the resonance should be proportional to $|\rho_0 - \rho_d|^2$. Now the nonresonant background reflection is $\rho_d = -1$, and we have $\rho_0 = 1$ at resonance for our system, we finally get the following expression for the time-averaged radiated power from the resonance $\langle P_r \rangle$:

$$\begin{aligned} \langle P_r \rangle &= |\rho_0 - \rho_d|^2 \cdot \int_{\text{u.c.}} d\vec{S} \cdot \frac{1}{2} \text{Re}((\vec{E}_0^{\text{PW},+})^* \times \vec{H}_0^{\text{PW},+}) \\ &= 2 \int_{\text{u.c.}} d\vec{S} \cdot \text{Re}((\vec{E}_0^{\text{PW},+})^* \times \vec{H}_0^{\text{PW},+}), \end{aligned} \quad (11)$$

where the surface integral is performed over a unit cell area on the top metallic layer. Again, Eq. (11) can be explicitly worked out (see Appendix B).

We now derive an analytical expression for the Q factor of the fundamental resonance discussed above based on the analytical expressions of U and P_r . However, the complete expression of the Q factor (Appendix B) appears quite complicated which obscures the inherent physics. The physics becomes much clearer if we consider the Q factor under the same two limits as discussed in Sec. IIIB. Specifically, we have

$$\begin{aligned} Q &= \frac{\sqrt{\varepsilon_d} \cdot \phi}{2 \sin^2(\phi)} + \frac{1}{h_d} \cdot \sum_{m \neq 0} \frac{\sqrt{\varepsilon_d} \cdot \phi \cdot m^2 G^2}{2[m^2 G^2 - \phi^2/h_d^2]^{3/2}} \\ &\cdot \frac{\sin^2(m\pi a/p)}{(m\pi a/p)^2}, \quad h_d/\lambda_0 \gg 1, \end{aligned} \quad (12A)$$

$$\begin{aligned} Q &= \frac{1}{2k_0 h_d} \cdot \sum_m \frac{\varepsilon_d k_0^2 \cdot [m^2 G^2 + \varepsilon_d k_0^2]}{[m^2 G^2 - \varepsilon_d k_0^2]^2} \\ &\cdot \frac{\sin^2(m\pi a/p)}{(m\pi a/p)^2}, \quad h_d/\lambda_0 \ll 1, \end{aligned} \quad (12B)$$

where $\phi = \sqrt{\varepsilon_d} \cdot k_0 h_d$ and $k_0 = \omega/c$ (see Appendix B).

Equations (12A) and (12B) again show distinct behaviors highlighting the differences between two types of resonances in two extreme limits. To check the validities of our derived formulas, we employed these formulas to calculate the Q factors as functions of h_d for a series of systems with $a/p = 1/15$ and ε_d fixed and then compared such analytical results with corresponding FDTD results and available experimental data on a certain set of samples. In both FDTD simulations and experiments, the Q factors are estimated by the formula $Q = \Delta f/f_0$ with Δf being the frequency intervals where Φ changes from -90° to 90° . Comparisons shown in Fig. 3 justified our analytical formulas and, more importantly, reveal the distinct behaviors of Q factors in two limits. In the case of a thick cavity, the Q factor is predominately dictated by the fundamental mode, while all high-order terms only contribute to a small correction term [see Eq. (12A)]. In fact, the first term in Eq. (12A) is precisely the Q factor

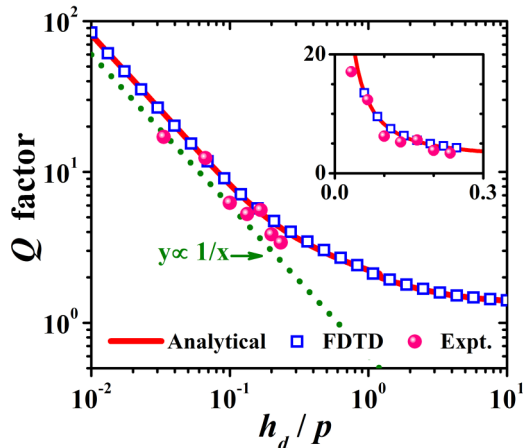


FIG. 3. Q factors for fundamental resonances in MIM systems with different spacer thickness h_d , obtained by experiments (solid circles), FDTD simulations (open squares), and our analytical formulas (solid lines). Inset shows a zoomed view of the region $h_d/p \in [0, 0.3]$. Other parameters are fixed as $a = 1$ mm, $p = 15$ mm, $h_m = 0.035$ mm, and $\varepsilon_d = 4.3$.

of a standard FP cavity (with a dielectric layer and PEC sheet) [28], while the second term in Eq. (12A) dies off in the limit of $h_d \rightarrow \infty$. In this limit, Q remains nearly a constant with increasing h_d since the propagation phase ϕ on resonance is nearly a constant. All these behaviors are consistent with the picture set up in the interference model [21]. However, the Q factor under the thin-cavity limit exhibits distinct behaviors. Similar to the discussions on the $\lambda_0 \sim h_d$ relationship, here not only the fundamental mode but also *all* high-order evanescent waves have *nearly equal* contributions to the Q factor [see Eq. (12B)]. Most importantly, now the Q factor is nearly inversely proportional to spacer thickness h_d , which is quite counterintuitive at first glance. Such an intriguing behavior can be explained by the significantly enhanced NFC in the $h_d \rightarrow 0$ limit. In such a case, the amplitudes of all modes exhibit the same inverse dependence on h_d , i.e., $c_m^\pm = \pm S_{m0}^{(3,2)} / S_{00}^{(1,2)} \cdot (ik_{m,z}^{\text{III}} h_d)^{-1}$, which means that the electric field is inversely proportional to h_d . Therefore, we have $U \propto E^2 \cdot V \propto (1/h_d)^2 \cdot h_d \propto 1/h_d$, and thus the Q factor must be inversely proportional to h_d in the thin-spacer region. The $Q \propto h_d^{-1}$ relation can also be understood as follows: as $h_d \rightarrow 0$, the cancellation between radiations from two metallic layers becomes better and better, and thus the resonance becomes darker and darker. Note here, we only considered the radiative Q factor which is divergent in the limit of $h_d \rightarrow 0$. In reality, the divergence of the total Q factor will be killed by the absorption and the total Q factor becomes finite in the limit of $h_d \rightarrow 0$.

D. Influences of a/p on the resonance properties

The resonance properties of an MIM system can also be modified by its lateral geometry (dictated by a/p in our model), as suggested by the derived formulas. To illustrate the role of a/p , we employed both FDTD simulations and the analytical formulas to numerically calculate both λ_0 and Q for two series of MIM systems (with different h_d) with varying

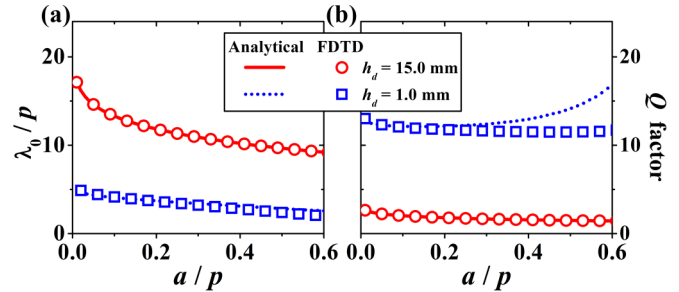


FIG. 4. (a) Resonance wavelength λ_0 and (b) the Q factor for the fundamental modes in MIM systems with different slit width a , obtained by FDTD simulations (symbols) and our analytical formulas (lines). Two sets of MIM systems with different spacer thickness ($h_d = 15$ mm and $h_d = 1$ mm) are studied, with other parameters fixed as $p = 15$ mm, $h_m = 0.035$ mm, and $\varepsilon_d = 4.3$.

a/p and a fixed $p = 15$ mm. As shown in Fig. 4, we found the parameter a/p only weakly modifies the resonance properties of such MIM systems, in consistency with the analytical formulas which only weakly depend on a/p . However, we emphasize that this conclusion is only valid for stripe-array pattern studied here.

It is worth noting that our analytical formulas (solid lines) work very well only in the region of $a/p \leq 0.3$, but the model predictions do have some deviations from the full-wave FDTD results as $a/p > 0.3$, particularly for the Q factors. The inherent reason is that when a/p increases, the single-mode approximation is no longer accurate since high-order waveguide modes inside the slits can be easily excited due to their nonnegligible overlapping with the incident wave.

IV. PROPERTIES OF HIGH-ORDER RESONANCES IN THICK-SPACER SYSTEMS

So far, the results presented in last sections are all for the fundamental resonance in MIM structures. However, our analytical formulas [i.e., Eq. (5)–(7)] are not restricted to the *fundamental* resonance but rather valid for *all* high-order resonances. In this section, we employ those formulas to examine the exotic behaviors of high-order resonances in such MIM structures, mainly focusing on their resonance wavelengths. We will show that fascinating new physics appears in MIM systems with larger h_d , due to the interplays between different mechanisms forming the resonances.

We first numerically solve Eq. (7) to obtain all resonance wavelengths of an MIM structure with a particular h_d and depict the obtained results versus h_d in Fig. 5(a) as thin white lines. To justify these analytical results, we next employ full-wave simulations to study the absorption spectra of the same set of MIM structures in which the permittivity of the dielectric spacer is assumed to exhibit a small imaginary part. Obviously, the absorption peaks just correspond to the resonances in the studied systems, as shown by the color map in Fig. 5(a). We note that the analytical solutions (lines) are in excellent agreement with full-wave simulation results (color map), which again justify our analytical formulas.

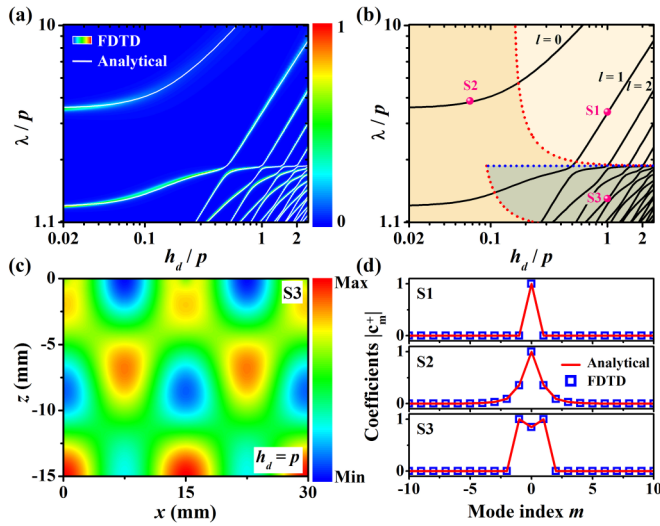


FIG. 5. (a) Absorption spectra (color map) of MIM systems (with $\epsilon_d = 4.3 + 0.02i$) with different spacer thicknesses h_d . White lines depict the resonance wavelengths of MIM systems versus their spacer thicknesses h_d , obtained by solving Eq. (13). (b) Replotting the analytical solutions of Eq. (13) (black lines) in a $\lambda \sim h_d$ phase diagram, which is now divided into three regimes by three boundary lines. Two red dotted lines are calculated by $h_d^{c,1} = \text{Im}(k_{1,z}^{\text{III}})^{-1}$ and $h_d^{c,2} = \text{Im}(k_{2,z}^{\text{III}})^{-1}$, respectively, and the blue horizontal line is calculated by $\lambda_c = \sqrt{\epsilon_d} \cdot p$. Solid circles (labeled by S1, S2, and S3) depict the locations of three selected resonances with field distributions shown in Figs. 2(c), 2(d) and 5(c), respectively. (c) FDTD-calculated $\text{Re}(H_y)$ field distribution on an arbitrary x - z plane in an MIM system with $h_d = 15$ mm at frequency 13.94 GHz [corresponding to the mode labeled as S3 in Fig. 5(b)]. (d) Relative contributions from different diffraction modes in three resonances labeled by S1, S2, and S3, obtained by Fourier transforming the FDTD-calculated patterns (squares) and the rigorous MEM (lines). For all MIM systems studied here, we fix $a = 1$ mm, $p = 15$ mm, $h_m = 0.035$ mm.

Figure 5(a) shows that the resonances exhibit intriguing behaviors, especially in the large- h_d region where interesting anticrossing phenomena [29] appears. To understand these unusual behaviors, we replot the analytical solutions in Fig. 5(b), where the whole space is divided into three regions by two different types of boundary lines. The two red dotted lines, calculated by the formulas $h_d^{c,1} = \text{Im}(k_{1,z}^{\text{III}})^{-1}$ and $h_d^{c,2} = \text{Im}(k_{2,z}^{\text{III}})^{-1}$, define the boundaries dictating whether the first/second evanescent modes can reach the metallic ground plane. Meanwhile, the blue horizontal line, defined by $\lambda_c = \sqrt{\epsilon_d} \cdot p$, divide the space into two regions; the first diffraction mode inside the spacer becomes propagating (evanescent) in the region of $\lambda < \lambda_c$ ($\lambda > \lambda_c$).

These boundary lines divide the whole space into three subregimes, each with distinct resonance properties. The right-up region is obviously a far-field dominated regime where only the fundamental mode inside the spacer is alive and all high-order diffraction modes are evanescent and thus only provide a correction to the reflection phase of the top metallic layer. Meanwhile, the left region is predominantly dictated by near fields in which high-order evanescent modes inside the spacer cannot be dropped and should be considered when

forming the resonance. Indeed, the fundamental resonance in an MIM system (the line labeled with $l = 0$) evolves continuously from an FP-like mode in the far-field-dominated regime to a lateral mode in the near-field-dominated regime as h_d decreases, consistent with the picture established in Sec. III.

The most intriguing region is the right-down corner, where both the fundamental mode and the *first* diffraction mode are *alive* inside the spacer, while at the same time all high-order evanescent modes *cannot* reach the ground plane. Using the same arguments in deriving Eq. (8), we found that now the resonance wavelengths should be determined by

$$Y_0^{\text{III}} |S_{00}^{(3,2)}|^2 \cot(k_{0,z}^{\text{III}} h_d) + 2Y_1^{\text{III}} |S_{10}^{(3,2)}|^2 \cot(k_{1,z}^{\text{III}} h_d) - i \sum_{|m|>1} Y_m^{\text{III}} |S_{m0}^{(3,2)}|^2 = l\pi, \quad l = 0, 1, 2, \dots \quad (13)$$

Equation (13) shows that two propagating modes are involved in forming the FP resonances in this regime, while all remaining evanescent modes contribute to a surface-related phase term. Therefore, such a regime is still dominated by far fields but now with two propagating modes involved in forming the FP resonances. We solved Eq. (13) analytically and found that the solutions (not shown) are in perfect agreement with the results shown in Figs. 5(a) and 5(b). Such a formula also helps us understand the fascinating resonance anticrossing behaviors [29] as shown in Figs. 5(a) and 5(b). For any l , we can always find two different solutions of Eq. (13) by adjusting the relative contributions from two propagating modes, while the same thing can never happen in the right-up regime where only one mode is alive [see Eq. (8)]. Figure 5(b) shows that there is an h_d -independent resonance at the boundary line $\lambda_c = \sqrt{\epsilon_d} \cdot p$ in the large- h_d limit. This phenomenon is closely related to “Wood’s anomalies” [30–32]. The physics is that an incident wave of this wavelength can excite a surface resonance on the top metallic layer, which is now interpreted as the spoof surface plasmon polariton of that layer.

To gain deeper understandings on the resonances in different regimes, we purposely select three representative examples from three regimes [labeled as S1, S2, and S3 in Fig. 5(b)], and then perform full-wave simulations to study their field distributions. Resonances labeled by S1 and S2 are just what we have studied in Sec. III, with their field distributions already depicted in Figs. 2(c) and 2(d), respectively. Figure 5(c) shows the field distribution of the resonance labeled by S3 selected from the right-down regime in Fig. 5(b). The field profile depicted in Fig. 5(c) clearly uncovers the two-mode hybridization nature of this resonance, since the field distribution does not exhibit a well-defined single k -vector, which is quite different from the S1 case depicted in Fig. 2(c). As a quantitative check, we perform Fourier transforms on these field patterns (i.e., Figs. 2(c), 2(d), and 5(c)) to retrieve the contributions from different diffraction modes. Figure 5(d) shows clearly that both the zero- and first-order diffraction modes are involved in forming the interference pattern in the S3 case, while essentially only the zero-order mode contributes to the resonance formation in the S1 case. Meanwhile, more diffraction modes are involved in forming the S2 resonance, although the contributions from high-order terms decay significantly. However, more and more high-order evanescent waves will be induced as h_d is reduced,

and such a trend becomes more dramatic as the spacer becomes thinner and thinner.

V. EXTENSION TO GENERAL SITUATIONS WITH COMPLEX LATERAL GEOMETRY

Although the results presented in the last sections are all based on a simple model with a stripe-array lateral geometry, we show in this section that the established physical pictures are general enough for MIM systems with more complex lateral geometries. In fact, the MEM established in Sec. II can be easily extended to study the MIM MTMs with two-dimensional (2D) microstructures. The coupled linear equations to determine all expansion coefficients are basically the same as Eq. (4), except that the sum should now be performed over all possible scattering directions and with two possible polarizations σ . However, in contrast to the stripe-array case, here the overlapping integrals cannot be analytically computed for 2D microstructures, since the related wave-functions of the Floquet eigenmodes in region II cannot be obtained analytically. Alternatively, one can compute these overlapping integrals numerically. Specifically, the overlapping integrals between the diffraction mode in Region I indexed by $\{n_x, n_y\}$ (with parallel wave vector $\vec{k}_{\parallel} = \vec{k}_{\parallel}^{\text{inc}} + n_x G_x \hat{x} + n_y G_y \hat{y}$, where G_x and G_y are reciprocal vectors along two directions) and the q th Floquet mode in Region II is represented as

$$S_{\{n_x, n_y\}, q}^{\sigma, (1,2)} = (S_{q, \{n_x, n_y\}}^{\sigma, (2,1)})^* = \frac{\int_{u.c.} dx dy (\vec{E}_{\{n_x, n_y\}}^{\sigma, \text{PW}})^* \cdot \vec{E}_q^{\text{Floquet}}}{\sqrt{\int_{u.c.} dx dy |\vec{E}_{\{n_x, n_y\}}^{\sigma, \text{PW}}|^2} \cdot \sqrt{\int_{u.c.} dx dy |\vec{E}_q^{\text{Floquet}}|^2}}. \quad (14)$$

Here, the integrals are performed within a unit-cell surface area with eigenwave functions $\vec{E}_q^{\text{Floquet}}$ computed by numerical simulations, and $S_{\{m_x, m_y\}, q}^{\sigma, (3,2)} = (S_{q, \{m_x, m_y\}}^{\sigma, (2,3)})^*$ has a similar definition.

Applying the same single-mode and thin metallic-layer approximations as in Sec. II, we arrive at the similar analytical solutions for MIM systems with 2D patterns. Without repeating those tedious but straightforward derivations, we emphasize here that all formulas are essentially the same as their 1D counterparts [e.g., Eqs. (5)–(13)], except that, here, the sums for scattering modes in Region III should be performed over two reciprocal indexes $\{n_x, n_y\}$ and polarization index σ . It is thus easy to expect that resonances in MIM MTMs with 2D complex microstructures exhibit similar crucial features as their 1D counterpart, as long as the two approximations mentioned above are still valid.

We choose two typical MIM systems with different 2D microstructures to study how their resonance properties (λ_0 and Q) of the fundamental resonance vary against the spacer thickness h_d . Without losing generality, we assume that the unit microstructure is an anisotropic metallic square in one sample [Fig. 6(a)] and a symmetrical cross in another one [Fig. 6(b)]. Figures 6(a) and 6(b) depict the FDTD-calculated electric field distributions of the fundamental Floquet modes in Region II of two systems, respectively. With these wave functions, we

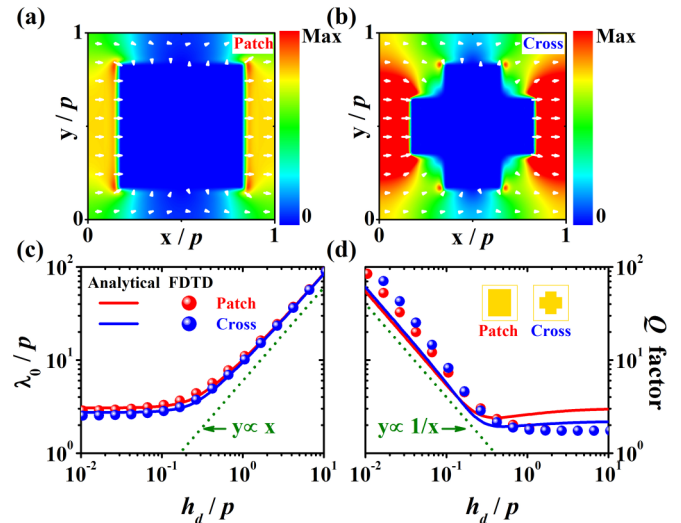


FIG. 6. FDTD-calculated \mathbf{E} -field distributions (with color/arrow representing the amplitude/direction of the field) of the fundamental modes inside Region II for MIM systems with top-layer unit-cell microstructures as (a) a metallic patch sized 10×12 mm and (b) a metallic cross with bar width 5 mm and bar length 10 mm. The periodicity of the pattern is 15 mm along two directions. Color and arrow represent the amplitude and direction of the local \mathbf{E} field. (c) Resonance wavelength λ_0 and (d) the Q factor of the fundamental resonance in MIM systems with different spacer thickness h_d , obtained by FDTD simulations (circles) and our analytical formulas (solid lines). Two series of MIM systems with different top-layer microstructures (i.e., patch and cross) are studied. Other parameters are $h_m = 0.035$ mm and $\varepsilon_d = 4.3$.

can calculate the involved S parameters according to Eq. (14) and then compute the essential properties of the resonances in such MIM structures. Solid lines in Fig. 6 are λ_0 and Q for the fundamental resonance in both structures as functions of their spacer thickness h_d , calculated by our analytical formulas. They are found to match quite well with FDTD simulations (circles). The $\lambda_0 \sim h_d$ and $Q \sim h_d$ curves for two MIM structures do deviate from each other slightly, but they surprisingly share the same universal laws as already discussed based on their 1D counterpart in Secs. II–III. The quantitative differences between these curves are caused by different values of their S parameters, which depend sensitively on the shape of the microstructures.

VI. CONCLUSION

To summarize, here, we present a systematic study on the resonances in MIM systems. We show that the fundamental resonance undergoes a transition from a FP-like vertical resonance to a lateral one as the spacer thickness shrinks. The underlying physics is that high-order evanescent waves, which die off in the multiple-scattering process and only contribute to a reflection phase correction in the thick-spacer limit, play very important roles to couple two metallic layers together as the spacer becomes thinner. Distinct from the thick-spacer limit where the resonance is basically a standard FP one, the resonance exhibits intriguing behaviors in the thin-spacer limit dictated by such NFC. In particular,

the resonance wavelength saturates at a certain value, and the quality factor of the resonance is inversely proportional to the spacer thickness, which are universal for such MIM systems independent of their lateral geometry. More fascinating hybridization behaviors appear for high-order resonances in thick-spacer MIM systems, due to interplays between different mechanisms forming the resonances. We derived a set of analytical formulas to describe such intriguing resonance behaviors and verified them by full-wave simulations and microwave experiments. Our paper not only offers a closed set of analytical expressions working for both near-field and far-field dominated cases, but more importantly, also provides a unified picture to understand the rich physics in such systems.

ACKNOWLEDGMENTS

This paper was supported by National Natural Science Foundation China (Grants No. 11474057 and No. 11174055), and the Ministry of Education of China (Grant No. B06011).

APPENDIX A: DERIVATION OF EQS. (4)–(6)

Matching the boundary conditions for \mathbf{E} field at the $z = h_m$ interface, we have

$$\begin{aligned} & \vec{E}_{0,\parallel}^{\text{PW},-} + \sum_n \rho_n \vec{E}_{n,\parallel}^{\text{PW},+} \\ &= \begin{cases} \sum_q (a_q^+ \vec{E}_{q,\parallel}^{\text{WG},+} + a_q^- \vec{E}_{q,\parallel}^{\text{WG},-}) & |x| \leq a/2 \\ 0 & |x| > a/2 \end{cases}. \end{aligned} \quad (\text{A1})$$

Using the orthonormal conditions $\int_{-p/2}^{p/2} (\vec{E}_{n,\parallel}^{\text{PW}})^* \cdot \vec{E}_{n',\parallel}^{\text{PW}} dx = \delta_{n,n'}$, we get

$$\delta_{n,0} + \rho_n = \sum_q S_{nq}^{(1,2)} [a_q^+ \exp(ik_{q,z}^{\text{II}} h_m) + a_q^- \exp(-ik_{q,z}^{\text{II}} h_m)], \quad (\text{A2})$$

where the coupling strengths are

$$\begin{aligned} S_{nq}^{(1,2)} &= \int_{-p/2}^{p/2} (\vec{E}_{n,\parallel}^{\text{PW}})^* \cdot \vec{E}_{q,\parallel}^{\text{WG}} dx \\ &= \frac{1}{2} \cdot \sqrt{a/p} \cdot \{ \sin c(n\pi \cdot a/p - q\pi/2 + k_{0,x} a/2) \\ &\quad + (-1)^q \cdot \sin c(n\pi \cdot a/p + q\pi/2 + k_{0,x} a/2) \}. \end{aligned} \quad (\text{A3})$$

Similarly, matching the boundary condition for the \mathbf{H} field at this interface, we have

$$\begin{aligned} & -Y_0^{\text{I}} E_0^{\text{PW},-} + \sum_n \rho_n Y_n^{\text{I}} \vec{E}_n^{\text{PW},+} \\ &= \sum_q Y_q^{\text{II}} (a_q^+ \vec{E}_q^{\text{WG},+} + a_q^- \vec{E}_q^{\text{WG},-}), \quad |x| < a/2. \end{aligned} \quad (\text{A4})$$

Now using the orthonormal conditions for the waveguide modes, $\int_{-a/2}^{a/2} (\vec{E}_{q,\parallel}^{\text{WG}})^* \cdot \vec{E}_{q',\parallel}^{\text{WG}} dx = \delta_{q,q'}$, we have

$$\begin{aligned} & \sum_n S_{qn}^{(2,1)} Y_n^{\text{I}} [\rho_n - \delta_{n,0}] \\ &= Y_q^{\text{II}} [a_q^+ \exp(ik_{q,z}^{\text{II}} h_m) - a_q^- \exp(-ik_{q,z}^{\text{II}} h_m)], \end{aligned} \quad (\text{A5})$$

where the overlapping integrals are $S_{qn}^{(2,1)} = \int_{-a/2}^{a/2} (\vec{E}_q^{\text{WG}})^* \cdot \vec{E}_n^{\text{PW}} dx = (S_{nq}^{(1,2)})^*$. Equations (A2) and (A5) are just the first two questions in Eq. (4) of the main text. Other equations in Eq. (4) can be derived in a similar way.

We now present the detailed derivations for Eqs. (5) and (6) in the main text. As discussed in Sec. III A, we can only retain the fundamental modes in regions I and II and assume that $h_m = 0$. Therefore, Eq. (4) can be simplified as

$$\begin{aligned} \rho_0 + 1 &= S_{00}^{(1,2)} (a_0^+ + a_0^-) \\ S_{00}^{(2,1)} Y_0^{\text{I}} (\rho_0 - 1) &= Y_0^{\text{II}} (a_0^+ - a_0^-) \\ c_m^+ + c_m^- &= S_{m0}^{(3,2)} (a_m^+ + a_m^-) \\ \sum_m S_{0m}^{(2,3)} Y_m^{\text{III}} [c_m^+ - c_m^-] &= Y_0^{\text{II}} (a_0^+ - a_0^-) \\ c_m^+ \exp(-ik_{m,z}^{\text{III}} h_d) + c_m^- \exp(ik_{m,z}^{\text{III}} h_d) &= 0. \end{aligned} \quad (\text{A6})$$

Solving Eq. (A6), we get an explicit expression for ρ_0 , which is precisely Eq. (5) in the main text.

APPENDIX B: DERIVATION OF THE Q FACTOR

The expansion coefficients for the EM wave inside Region III can be obtained from directly solving Eq. (A6)

$$c_m^\pm = 2S_{m0}^{(3,2)} / S_{00}^{(1,2)} \cdot [1 - \exp(\mp 2ik_{m,z}^{\text{III}} h_d)]^{-1}. \quad (\text{B1})$$

With Eq. (B1), we can easily calculate $\langle U \rangle$. For example, the time-averaged energy stored in the E_x field is

$$\begin{aligned} \langle U_{E_x} \rangle &= \frac{1}{4} \varepsilon_d \varepsilon_0 \text{Re} \left(\int_{u.c.} d\tau E_x^* \cdot E_x \right) \\ &= \frac{1}{4} \varepsilon_d \varepsilon_0 \text{Re} \left\{ \int_{u.c.} d\tau \left(\sum_m (c_m^{+,*} \vec{E}_m^{\text{SC},+,*} + c_m^{-,*} \vec{E}_m^{\text{SC},-,*}) \right) \cdot \left(\sum_{m'} (c_{m'}^+ \vec{E}_{m'}^{\text{SC},+} + c_{m'}^- \vec{E}_{m'}^{\text{SC},-}) \right) \right\} \\ &= \varepsilon_d \varepsilon_0 h_d \sum_m \frac{(S_{m0}^{(3,2)})^2}{(S_{00}^{(1,2)})^2} \cdot \left(\frac{1}{2 \sin^2(k_{m,z}^{\text{III}} h_d)} - \frac{1}{2k_{m,z}^{\text{III}} h_d} \cot(k_{m,z}^{\text{III}} h_d) \right) \end{aligned} \quad (\text{B2})$$

Similarly, the energies stored in other field components are

$$\langle U_{Ez} \rangle = \varepsilon_d \varepsilon_0 h_d \sum_m \frac{(k_{m,x}^{\text{III}})^2}{(k_{m,z}^{\text{III}})^2} \cdot \frac{(S_{m0}^{(3,2)})^2}{(S_{00}^{(1,2)})^2} \cdot \left(\frac{1}{2 \sin^2(k_{m,z}^{\text{III}} h_d)} + \frac{1}{2 k_{m,z}^{\text{III}} h_d} \cot(k_{m,z}^{\text{III}} h_d) \right), \quad (\text{B3})$$

$$\langle U_{Hy} \rangle = \varepsilon_d \varepsilon_0 h_d \sum_m \frac{(k_0^{\text{III}})^2}{(k_{m,z}^{\text{III}})^2} \cdot \frac{(S_{m0}^{(3,2)})^2}{(S_{00}^{(1,2)})^2} \cdot \left(\frac{1}{2 \sin^2(k_{m,z}^{\text{III}} h_d)} + \frac{1}{2 k_{m,z}^{\text{III}} h_d} \cot(k_{m,z}^{\text{III}} h_d) \right). \quad (\text{B4})$$

Now we evaluate the time-averaged radiated power $\langle P_r \rangle$. A straightforward calculation on Eq. (11) yields

$$\langle P_r \rangle = |\rho_0 - \rho_d|^2 \cdot \int_{u.c.} d\vec{S} \cdot \frac{1}{2} \text{Re}(\vec{E}_0^{PW,+*} \times \vec{H}_0^{PW,+}) = 2 \frac{\omega \varepsilon_0}{k_{0,z}^{\text{I}}}. \quad (\text{B5})$$

Thus, the Q factor is found to be

$$\begin{aligned} Q &= \frac{2\pi f_c \langle U \rangle}{\langle P_r \rangle} \Big|_{f_c} = \frac{1}{2} k_{0,z}^{\text{I}} \varepsilon_0^{-1} \langle U \rangle \Big|_{f_c} \\ &= \frac{1}{2} \varepsilon_d k_{0,z}^{\text{I}} h_d \sum_m \frac{(S_{m0}^{(3,2)})^2}{(S_{00}^{(1,2)})^2} \cdot \left\{ \frac{(k_0^{\text{III}})^2}{(k_{m,z}^{\text{III}})^2} \cdot \frac{1}{\sin^2(k_{m,z}^{\text{III}} h_d)} + \frac{(k_{m,x}^{\text{III}})^2}{(k_{m,z}^{\text{III}})^2} \cdot \frac{1}{k_{m,z}^{\text{III}} h_d} \cot(k_{m,z}^{\text{III}} h_d) \right\}. \end{aligned} \quad (\text{B6})$$

While Eq. (B6) is valid for general cases, it is too complicated. We can simplify Eq. (B6) in the limits of thick- and thin-spacer thickness under normal incidence. In the case of $h_d/\lambda \gg 1$, for all modes with $m \neq 0$, we have $1/\sin^2(k_{m,z}^{\text{III}} h_d) \approx 0$ and $\cot(k_{m,z}^{\text{III}} h_d) \approx -i$, so that the Q factor can be simplified as

$$\begin{aligned} Q &= \frac{\varepsilon_d k_0 h_d}{2 \sin^2(k_{0,z}^{\text{III}} h_d)} - \frac{1}{2} \varepsilon_d k_0 h_d \cdot \sum_m \frac{\sin^2(m\pi a/p)}{(m\pi a/p)^2} \cdot \frac{m^2 G^2}{(k_{m,z}^{\text{III}})^2} \cdot \frac{1}{k_{m,z}^{\text{III}} h_d} i \\ &= \frac{\sqrt{\varepsilon_d} \cdot \phi}{2 \sin^2(\phi)} + \frac{1}{h_d} \cdot \sum_{m \neq 0} \frac{\sqrt{\varepsilon_d} \cdot \phi \cdot m^2 G^2}{2 [m^2 G^2 - \phi^2/h_d^2]^{3/2}} \cdot \frac{\sin^2(m\pi a/p)}{(m\pi a/p)^2}. \end{aligned} \quad (\text{B7})$$

Equation (B7) is precisely Eq. (12A) in the main text. On the other hand, in the limit of $h_d/\lambda \ll 1$, we have $1/\sin(k_{m,z}^{\text{III}} h_d) \approx \cot(k_{m,z}^{\text{III}} h_d) \approx 1/(k_{m,z}^{\text{III}} h_d)$, so that the Q factor can be simplified as

$$\begin{aligned} Q &= \frac{1}{2} \varepsilon_d k_0 h_d \sum_m \frac{\sin^2(m\pi a/p)}{(m\pi a/p)^2} \cdot \left\{ \frac{\varepsilon_d k_0^2}{(k_{m,z}^{\text{III}})^2} \cdot \frac{1}{(k_{m,z}^{\text{III}} h_d)^2} + \frac{m^2 G^2}{(k_{m,z}^{\text{III}})^2} \cdot \frac{1}{k_{m,z}^{\text{III}} h_d} \cdot \frac{1}{k_{m,z}^{\text{III}} h_d} \right\} \\ &= \frac{1}{2 k_0 h_d} \cdot \sum_m \frac{\varepsilon_d k_0^2 \cdot [m^2 G^2 + \varepsilon_d k_0^2]}{[m^2 G^2 - \varepsilon_d k_0^2]^2} \cdot \frac{\sin^2(m\pi a/p)}{(m\pi a/p)^2}. \end{aligned} \quad (\text{B8})$$

Equation (8) is precisely Eq. (12B) in the main text.

-
- [1] D. R. Smith, W. J. Padilla, D. C. Vier, S. C. Nemat-Nasser, and S. Schultz, *Phys. Rev. Lett.* **84**, 4184 (2000).
 [2] R. A. Shelby, D. R. Smith, and S. Schultz, *Science* **292**, 77 (2001).
 [3] J. B. Pendry, *Phys. Rev. Lett.* **85**, 3966 (2000).
 [4] N. Fang, H. Lee, C. Sun, and X. Zhang, *Science* **308**, 534 (2005).
 [5] J. Hao, Y. Yuan, L. Ran, T. Jiang, J. A. Kong, C. T. Chan, and L. Zhou, *Phys. Rev. Lett.* **99**, 063908 (2007).
 [6] J. Hao, Q. Ren, Z. An, X. Huang, Z. Chen, M. Qiu, and L. Zhou, *Phys. Rev. A* **80**, 023807 (2009).
 [7] N. K. Grady, J. E. Heyes, D. R. Chowdhury, Y. Zeng, M. T. Reiten, A. K. Azad, A. J. Taylor, D. A. R. Dalvit, and H.T. Chen, *Science* **340**, 1304 (2013).
 [8] N. I. Landy, S. Sajuyigbe, J. J. Mock, D. R. Smith, and W. J. Padilla, *Phys. Rev. Lett.* **100**, 207402 (2008).
 [9] T. Hu, C. M. Bingham, A. C. Strikwerda, D. Pilon, D. Shrekenhamer, N. I. Landy, K. Fan, X. Zhang, W. J. Padilla, and R. D. Averitt, *Phys. Rev. B* **78**, 241103 (2008).
 [10] N. Liu, M. Martin, W. Thomas, H. Mario, and G. Harald, *Nano Lett.* **10**, 2342 (2010).
 [11] N. Yu, P. Genevet, M. A. Kats, F. Aieta, J.-P. Tetienne, F. Capasso, and Z. Gaburro, *Science* **334**, 333 (2011).
 [12] S. Sun, Q. He, S. Xiao, Q. Xu, X. Li, and L. Zhou, *Nat. Mater.* **11**, 426 (2012).
 [13] A. Pors, M. G. Nielsen, R. L. Eriksen, and S. I. Bozhevolnyi, *Nano Lett.* **13**, 829 (2013).
 [14] A. S. Roberts, A. Pors, O. Albrektsen, and S. I. Bozhevolnyi, *Nano Lett.* **14**, 783 (2014).
 [15] W. T. Chen, K. Y. Yang, C. M. Wang, Y. W. Huang, G. Sun, I. D. Chiang, C. Y. Liao, W. L. Hsu, H.T. Lin, S. I. Sun, L. Zhou, A. Q. Liu, and D. P. Tsai, *Nano Lett.* **14**, 225 (2014).

- [16] A. Pors, M. G. Nielsen, and S. I. Bozhevolnyi, *Nano Lett.* **15**, 791 (2015).
- [17] J. B. Pendry, A. J. Holden, D. J. Robbins, and W. J. Stewart, *IEEE Trans. Microwave Theory Tech.* **47**, 2075 (1999).
- [18] V. M. Shalaev, W. Cai, U. K. Chettiar, H.-K. Yuan, A. K. Sarychev, V. P. Drachev, and A. V. Kildishev, *Opt. Lett.* **30**, 3356 (2005).
- [19] S. Dan, L. Zhang, R.F.J. Broas, N.G. Alexopolous, and E. Yablonovitch, *IEEE Trans. Microwave Theory Tech.* **47**, 2059 (1999).
- [20] J. Hao, L. Zhou, and C.T. Chan, *Appl. Phys. A* **87**, 281 (2007).
- [21] H.T. Chen, *Opt. Express* **20**, 7165 (2012).
- [22] R. Ameling and H. Giessen, *Laser Photonics Rev.* **7**, 141 (2013).
- [23] F. J. Garcia-Vidal, L. Martin-Moreno, and J. B. Pendry, *J. Opt. A: Pure Appl. Opt.* **7**, S97 (2005).
- [24] S. Xiao, Q. He, X. Huang, and L. Zhou, *Metamaterials* **5**, 112 (2011).
- [25] J. Bravo-Abad, F. J. García-Vidal, and L. Martín-Moreno, *Phys. Rev. Lett.* **93**, 227401 (2004).
- [26] Finite-difference-time-domain simulations demonstrated that the reflection properties of such MIM samples do not change obviously as we change the incident angle from 0° to 10° .
- [27] J. R. d. Lasson, P. T. Kristensen, J. Mork, and N. Gregersen, *J. Opt. Soc. Am. A* **31**, 2142 (2014).
- [28] S.G. Lipson, H. Lipson, and D.S. Tannhauser, *Optical Physics*, 3rd ed. (London: Cambridge U.P., 1995), p. 248.
- [29] T. Weiss, N. A. Gippius, G. Granet, S. G. Tikhodeev, R. Taubert, L. Fu, H. Schweizer, H. Giessen, *Photonics and Nanostructures* **9**, 390 (2011).
- [30] R. W. Wood, *Phylos. Mag.* **4**, 396 (1902).
- [31] U. Fano, *J. Opt. Soc. Am.* **31**, 213 (1941).
- [32] A. Hessel and A. A. Oliner, *Appl. Opt.* **4**, 1275 (1965).